CALPHAD-assisted development of *in-situ* nanocrystallised melt-spun Co-Fe-B alloy with high B_s (1.57 T)

Hasan Ahmadian Baghbaderani [a,b,*], Ansar Masood [a], Kenny L. Alvarez [c], Cian Ó Mathúna [a,d], Paul McCloskey [a], Plamen Stamenov [a,b]

[a] *Microsystems Centre, Tyndall National Institute, University College Cork, Cork, Ireland*
[b] *School of Physics and CRANN, Trinity College, Dublin 2, Ireland*
[c] *CEIT-Basque Research and Technology Alliance (BRTA), Manuel Lardizabal 15, 20018 Donostia-San Sebastián, Spain*
[d] *School of Electrical and Electronic Engineering, University College Cork, Cork, Ireland*

ARTICLE INFO

ABSTRACT

A thermodynamics-based approach, Calculation of Phase Diagram (CALPHAD), combined with topological instability parameters are proposed and experimentally evaluated, in order to optimise *in-situ* nanocrystallisation of rapidly quenched CoFeB alloys and exploit their remarkable B_s = 1.57 T. The high M_s of the alloy is attributed to the precipitation of the metastable Co_7Fe_3 nanocrystalline phase dispersed heterogeneously in the amorphous matrix. High M_s of Co_7Fe_3 phase can also be inferred from the high hyperfine magnetic field of the Fe nuclei deduced from Mössbauer spectra. It is worth noting that the *in-situ* nanocrystallisation is a volume phenomenon, instead of surface crystallisation at the air-side of ribbons owning to lower cooling rates. We judge, based on nucleation theory, that the formation of the metastable phase is kinetically favoured, when compared to the equilibrium phases, hence promoting the high M_s, when compared with conventional Co-rich amorphous alloys. The local atomic order of nanocrystallised phase was confirmed by X-ray and electron diffraction techniques. Using Mössbauer spectroscopy and the extracted distribution of the hyperfine magnetic field, it is asserted that cobalt atoms form clusters, as they attract each other to form ordered structures, and boron atoms undergo only short-range ordering, likely due to covalent bond formation, governed by the size and electronegativity differences with the atoms in the amorphous matrix. We suggest the proposed CALPHAD-assisted design of nanostructured alloys, along with an *in-situ* nanocrystallisation, provides a practical scheme to develop novel functional alloys with the best possible balance of coercivity and saturation, exclusively aimed for a high-tech application.

1. Introduction

The design of multifunctional materials is always prompted by an ever-increasing demand of advanced systems functionality: examples include miniaturised electronic devices, ultra-fast computational and communication capabilities, and ultra-high density data storage media. Sensors, actuators, and nano-micro-electromechanical systems (NEMS-MEMS) already integrate multifunctional materials and smart structures [1,2]. In this context, state-of-the-art magnetic materials, ranging from ultra-soft (Fe- and Co-rich amorphous alloys) to semi-hard (FePt-based) to permanent magnets (NdFeB-type), play a

vital role in designing smart and high-performance systems, including efficient power conversion [3–6], ultra-high density data storage media, and clean energy generation [7]. Amorphous magnetic alloys are well-known for their soft magnetic performance, high corrosion resistance, exceptional mechanical toughness and tensile strength, thanks to their unique disordered atomic structure to support this excellent combination of properties [8]. Particularly, CoFe-based alloys are of significant importance, due to their broad range of industrial applications, including data storage (*e.g.*, MRAM) and integrated power conversion (*e.g.*, PwrSoc) concepts [9]. However, the random atomic distribution in CoFe amorphous alloys contributes to the lower M_s, which eventually reduces their functionality for high magnetic flux applications. It is envisaged that the formation of nanocrystalline ordered phase in CoFe alloys is beneficial to enhance the M_s. Particularly, chemically ordered Co_7Fe_3 with CsCl structure has remained a focus of extensive research due to its high M_s and good

* Corresponding author at: Microsystems Centre, Tyndall National Institute, University College Cork, Cork, Ireland.
E-mail addresses: hbaghbaderani@ucc.ie, ahmadiah@tcd.ie (H. Ahmadian Baghbaderani).

chemical stability [10,11]. However, bare CoFe bimetallic nano-particles are highly pyrophoric in nature; alloys exposed to air result in the formation of the corresponding oxides. Thus, the ease of oxidation, their potential toxicity and intrinsically low relative density, hinder their functionality and hence stimulate developing alternative routes to grow the nominal phase and to materialise the advantages of the high-flux density CoFe-based alloys [11].

One of the alternative routes to developing the nanocrystalline alloys is a post-annealing of rapidly quenched amorphous precursors at elevated temperatures. However, nanocrystallisation of amorphous alloys is a multi-step process and requires a special scheme (additives and cooling rate) to control the nucleation and grain growth process of a particular phase. In a first step, high purity transition metals along with different glass formers are melt-spun to fabricate the amorphous precursors. As a second step, heat treatment is performed, in order to precipitate the nanocrystalline phases. However, the growth of a particular phase, with optimal performance is challenging. In addition, the heat treatment process (of nanocrystallisation) causes the embrittlement of the ribbons and, therefore, deteriorates the manufacturability in subsequent procedures [12]. An alternative approach to synthesise nanostructured alloys without post heat treatment is "*in-situ* nanocrystallisation" using rapid-quenching. However, this requires a careful design of alloy composition, with low or moderate amorphisation capability (AMC) to avoid both, vitrification into a glassy state, or precipitation into a fully crystalline state, during the rapid-quenching [13]. Further, the volumetric precipitation of the nanocrystalline phase is essential to promote, instead of surface crystallisation of the melt-spun ribbons, due to lower cooling rates at the air/gas-exposed side of the ribbons. To synthesise an optimised alloy, using *in-situ* nanocrystallisation approach, the prediction of AMC by calculation of the phase diagram (CALPHAD), combined with the topological instability parameter (λ), based on configurational entropies, estimated by mismatch factors, is established as an essential tool. Similar method is also well-proven in the optimisation of the glass forming ability of Fe- and Zr-based glassy alloys [14]. A number of glass-forming criteria, based on the different phase transition temperatures such as T_g (glass transition temperature), T_x (onset crystallisation temperature), T_l (onset liquidus temperature) and T_m (melting temperature), can be calculated and combined together with λ to predict the AMC of alloys. The room temperature amorphous phase is also thought to have the long-range disorder, which is mainly contributed by mismatch and configurational entropies, as estimated by mismatch factors [15]. Using a predictive modelling approach, one can design the alloys with moderate AMC, in order to fabricate nanocrystalline structures, when using rapid quenching, without post heat treatment. Thus, one can benefit from the high M_s of the bimetallic phase, in the form of Co_7Fe_3 nano-grains embedded in an amorphous matrix, formed *in-situ* with no consecutive thermal treatment.

In this work, thermodynamic parameters, predicted by the CALPHAD approach, and the topological instability criteria, λ, are considered to design the Co-Fe-B alloy with a moderate AMC and evaluate the formation of *in-situ* nanocrystalline structures of a CoFe-based alloy with high M_s using rapid-quenching. The very-high B_s (1.57 T) of the as-quenched alloy is clearly attributed to the formation of the Co_7Fe_3 nanostructured phase, which is dispersed heterogeneously in the amorphous matrix, throughout the volume of the melt-spun ribbons. The latter are subjected to detailed structural investigations, using XRD, TEM, and Mössbauer spectroscopy. Based on the compositional maps of the relevant parameters, a model is proposed to enhance the probability of *in-situ* nanocrystallisation, by adjusting the different thermodynamic and topological parameters.

2. Experimental methods

The equilibrium phase diagram of Co-Fe-B is thermodynamically modelled using Pandat™ software (version 2019). The cobalt-based thermodynamic database of the software is utilised to predict the enthalpy of mixing, the liquidus temperature and possible equilibrium and non-equilibrium phases at room temperature for $Co_{70}Fe_{17.5}B_{12.5}$ (atomic %) composition. To melt-spin the nominal alloy composition, first, the desired quantities of each element are weighed out using a standard microbalance to a precision of ~0.2 mg to make a 5 g ingot. The starting materials are Co pieces 99.5% trace metals basis (TMB), Fe chips 99.98% (TMB), and boron crystalline pieces 99.7%, all sourced from Sigma Aldrich. The alloy is prepared by arc-melting in high purity argon. Heating up occurs from an electric arc, which is created between a copper electrode and sharp welding tip (2% thoriated red-tungsten). The elements to be melted are contained within a water-cooled copper hearth. In general, the lower melting point elements are placed under those of higher melting point, except for boron, which is placed at the bottom of the hearth in an adjusted excess amount, in order to retain stoichiometry. The ingots are flipped and re-melted eight times to ensure homogeneity and a uniform lustre. As a precaution, high purity titanium (in a separate hearth) is used as a getter for oxygen.

Ribbons are subsequently produced by induction melting and melt-spinning the arc-melted ingots (in 1 g batch) in an argon atmosphere. An argon jet (at an overpressure of 0.7 bar) is used to eject the molten liquid contained in a fused silica vial. Typical experimental parameters and conditions applied are quartz vial of 60 mm length, 8 mm inner diameter and 0.5 mm diameter orifice, a nozzle to wheel angle of 10° from the perpendicular, a nozzle to wheel separation of ~0.1 mm, wheel diameter of 90 mm and a wheel speed of 80 m/s. Using the as-mentioned conditions, ribbons of ~14 µm thickness and ~1 mm width are obtained.

The X-ray powder diffraction (XRD) data of the melt-spun ribbons are collected using a Phillips PANalytical X'pert Pro diffractometer, with an operational wavelength of 1.5405 Å (Cu-Kα anode and a Ni filter). For transmission electron microscopy (TEM) analysis, each selected ribbon is first processed using a focused ion beam microscope (FEI Quanta 3D FEG). A protective metallic (Pt-based) layer is deposited on the surface before milling to create an ultrathin lamella, and two stair-step FIB trenches are cut at both sides of the area of interest. Next, the specimen is further thinned to less than 1 µm in thickness. Final milling down to less than 100 nm is carried out by employing successively lower voltages up to 2 kV. The obtained lamellae are removed using a micromanipulator and welded to a Cu grid suitable for transmission electron microscopy (TEM) analysis. TEM imaging of the ultrathin lamellae is performed using a JEOL JEM-2100F (S) TEM microscope operating at 200 kV with a LaB$_6$ filament. In addition, the coercivity and anisotropy field of the ribbons, along their length, is measured using a *B-H* loop tracer (at f = 10 Hz) with a maximum magnetic field of 0.1 Tesla. Additionally, the M_s of the sample is studied by superconducting quantum interference device (SQUID-based) magnetometry (MPMS 5XL, Quantum Design, USA) at RT in fields of up to $\mu_0 H \leq 2$ T. Room temperature transmission Mössbauer spectra are collected using a conventional constant acceleration spectrometer with ^{57}Co sealed in the Rh matrix source. In this geometry, the γ-ray direction is perpendicular to the ribbon plane. The electrical resistivity measurements were carried out at room temperature using a DC four-probe method with fixed distances (*i.e.*, 1 mm) between the four probes. The potential drop is picked up on the 22 mm long specimen, with an equivalent resistance error of ±0.001 Ω. All samples are measured at six different voltage levels, and the data is regressed upon, in order to diminish the role of contact non-linearities and heating.

3. Results and discussions

3.1. CALPHAD-assisted alloy design

Several criteria have been established to evaluate the amorphisation capability of rapidly quenched metallic alloy systems [14], suggesting how the disordered atomic structure in metallic alloys can be preserved on vitrification with the lowest possible cooling rates (defined as critical cooling rate, a well-known measure of the AMC of the amorphous alloys) [14]. However, all parameters are empirical and based on trial-and-error. More recently, there has been some interest to an alternative evaluation of the AMC criterion for the amorphous alloys, using the CALPHAD approach, augmented by the topological instability factor λ. This predictive model of amorphisation has worked well, in a couple of examples, hence suggesting a working alternative for the prediction of the glass forming ability of alloys [16,17]. Interestingly, this criterion can be useful, when there is an interest in the growth of metastable nanocrystalline structures using the rapid quenching process. The alloy composition can be tuned, in a particular region of the phase diagram, where λ is not favourable for high AMC, and hence, the chance of precipitation of the desired metastable phases increased, during vitrification. Keeping this in mind, the following thermodynamic parameters, along with λ, are scrutinised in a specific region of the phase diagram to regulate the moderate AMC and design an alloy, in which the metastable nanocrystalline phase precipitates during melt spinning process.

3.1.1. Liquidus temperature

When a liquid melt is cooled down from the liquid state to a temperature below the T_g, the viscosity of the melt increases to a high value, and consequently, glass is vitrified. The effective viscosity at T_g is known to be fixed at 10^{12} Pa.s, as initially suggested by Turnbull [18], which is originally based on the kinetics of crystal nucleation and the viscosity of the melts. It suggests that the ratio of T_g to the liquidus temperature, T_l, also well-known as reduced glass transition temperature, T_{rg} (Eq. 1), can be a good indicator of the susceptibility to amorphisation of the alloys. The higher the value of T_{rg}, the higher is the viscosity, and therefore the alloy melt could easily be solidified into the amorphous state, at a lower critical cooling rate. In other words, an alloy composition with a high value of T_g and a low value of T_l is preferable to promote high amorphisation capability.

$$T_{rg} = \frac{T_g}{T_l} \tag{1}$$

Further, it has been experimentally proven that the value of T_g changes slowly with solute contents. On the other hand, T_l of an alloy usually decreases with increasing solute content in most of the alloy systems. Particularly, phase diagrams of some alloy systems show that liquidus curves drop very steeply with solute content [19]. Furthermore, an alloy with a eutectic temperature significantly lower than the melting points of the individual elements is referred to as a "deep" eutectic. In such cases, the T_{rg} value around the "deep" eutectic composition is a strong function of the alloy composition and exhibits its highest value at the eutectic composition. Therefore, it should be possible to quench this alloy composition easily into a glassy state.

On the other hand, if the liquidus temperature of an alloy also decreases slowly with the solute content, then the T_{rg} value at the eutectic composition may not be high. In such a situation, it will be challenging to produce such an alloy in the glassy state. Thus, the Turnbull criterion of high T_{rg} and deep eutectics converge at the deep eutectic compositions [14]. Fig. 1 illustrates the liquidus projection in the Co-Fe-B phase diagram, in which the liquidus isotherms are
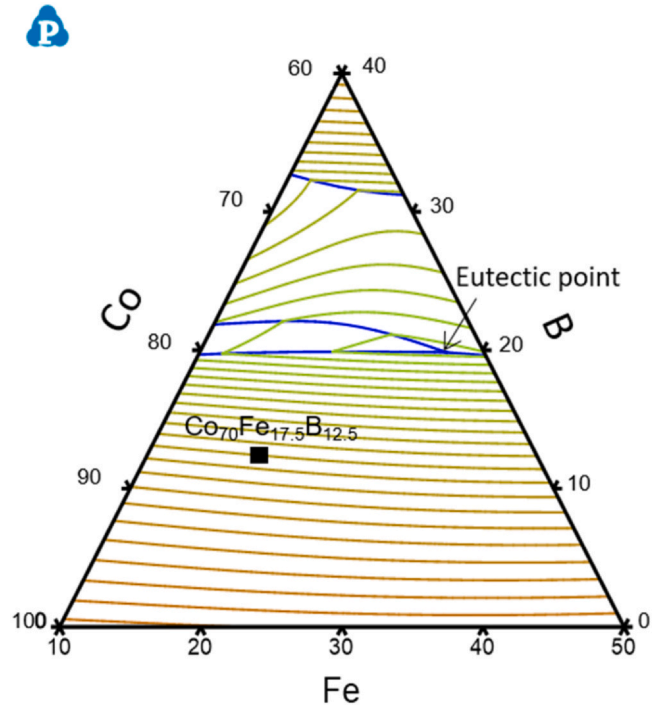

Fig. 1. Liquidus surface projection of the Co-Fe-B phase diagram in the Co-rich zone calculated by CALPHAD. The red and green lines show isothermal lines with a difference of 25 °C, decreasing toward the eutectic point.

shown every 25 °C decreasing towards the eutectic point. The composition is chosen to be in the region in which the liquidus temperature is approximately in the middle of the highest liquidus temperature, shown by brown and red coloured isotherms towards the horizontal axis, and the deep eutectic point at 1051 °C (Fig. 1). The main reason for choosing an alloy composition with middle-range T_l is to obtain a moderate AMC to *in-situ* nanocrystallise the alloy using melt-spinning.

3.1.2. Enthalpy of mixing

According to Inoue's empirical rule [20], the enthalpy of mixing, ΔH_{mix}, significantly favours the formation of amorphous structure and is a good measure of the AMC. It has been suggested that a significant negative heat of mixing would lead to an increase in the energy barrier at the liquid-solid interface, and a decrease in the atomic diffusivity through the growth interface. The large mixing enthalpy would be expected to lower the effective mobilities of even the lightest species (*i.e.* boron) in the melt, which following Einstein's relation, would in turn increase the effective melt viscosity [21]. Thus, the more negative the ΔH_{mix}, the higher the AMC of an alloy [2,4].

The chemical mixing enthalpy is calculated according to Eq. (2) based on the extended regular solution model [22]:

$$\Delta H_{mix} = \Omega_{CoFe} c_{Co} c_{Fe} + \Omega_{CoB} c_{Co} c_B + \Omega_{FeB} c_{Fe} c_B \tag{2}$$

where Ω_{ij} is the regular solution interaction parameter between i and j elements, which can be expressed by the mixing enthalpy of binary alloys ($\Omega_{ij} = 4\Delta H_{mix}^{ij}$), and c_i is the molar fraction of the i element [23]. Ternary diagram of enthalpy of mixing in the Co-Fe-B system is presented in Fig. 2. The labelled alloy composition is chosen to display an enthalpy of mixing, −9.56 kJ/mol, which is the region where this parameter is neither highly negative, towards the boron-rich alloys, nor extremely positive towards the Fe-rich alloy compositions. The moderate ΔH_{mix} could result in a moderate AMC, which can lead to the *in-situ* fabrication of nanocrystallised alloy.
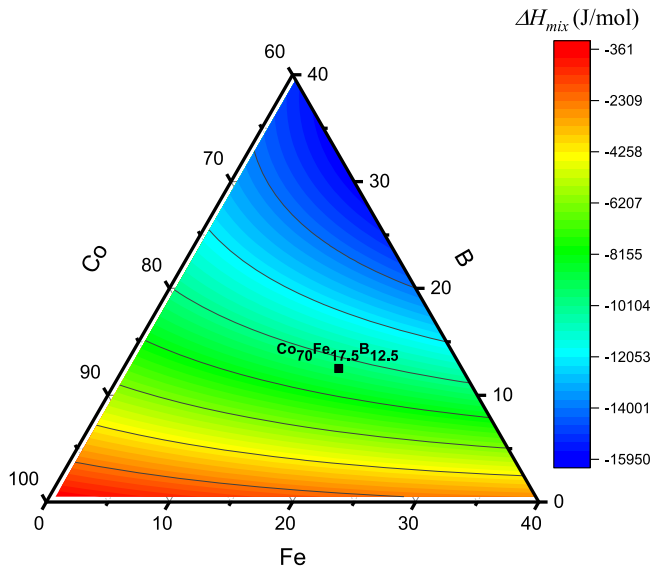
Fig. 2. Color map of enthalpy of mixing in the Co-rich corner in the Co-Fe-B system.

3.1.3. Atomic mismatch factor

In addition to thermodynamic parameters, a topological parameter has also been used to predict the amorphisation capability of a metallic system. This effect has long been accounted for the empirical requirement for constituent atoms with at least a 12% size difference [14]. A more continuous approach to the question of topology has been linked to a critical lattice strain, caused by the volumetric mismatch of the species, required to suppress crystallisation. This concept was developed by Sá Lisboa et al. [24] through the atomic mismatch factor, λ in multicomponent systems [16],

$$\lambda = \sum_{i=B}^{Z} c_i \left| \left(\left(\frac{r_i}{r_A} \right) \right)^3 - 1 \right| \tag{3}$$

where i denotes the different solutes B to Z in matrix A, c_i is the concentration of solute i in matrix A (mol%), r_i is the solute atomic radius (nm), and r_A is the solvent atomic radius (nm).

Yan et al. [25] noted that optimal glass-forming happens at $\lambda = 0.18$ for several investigated multicomponent systems. When assuming that an amorphous material is made up of numerous clusters of icosahedra, the packing efficiency peaks at $\lambda = 0.18$. It can also be inferred from [26] that $\lambda = 0.18 \pm 0.04$ can be considered as a region with a reasonably high AMC in several distinct alloy systems. Thus, the alloy composition is chosen on the boundary of the region with optimum λ to show moderate AMC, as shown in Fig. 3 where the λ-lines are superimposed in the Co-Fe-B phase diagram, to *in-situ* nanocrystalline the alloy during quenching. In other words, based on the λ parameter, the AMC of the alloy is lower as compared to the alloys inside the green region, but considerably higher when compared to the alloys outside the green region. This moderate (tuned) AMC can lead to *in-situ* nanocrystallisation of the alloy during melt spinning.

Thus, the proposed predictive model of *in-situ* nanocrystallisation encompasses both, the thermodynamic and topological, aspects of the alloy system and amalgamates the information on the compositional regions with middle-range T_l, enthalpy of mixing and atomic mismatch factor for the amorphous microstructure. It predicts moderate values of AMC, by identifying the region of interest using T_l, ΔH^{mix}, and the λ-factor on the phase diagram. It will be shown that the rapid quenching of alloys with tuned AMC can result in an *in-situ* nanocrystalline alloy.
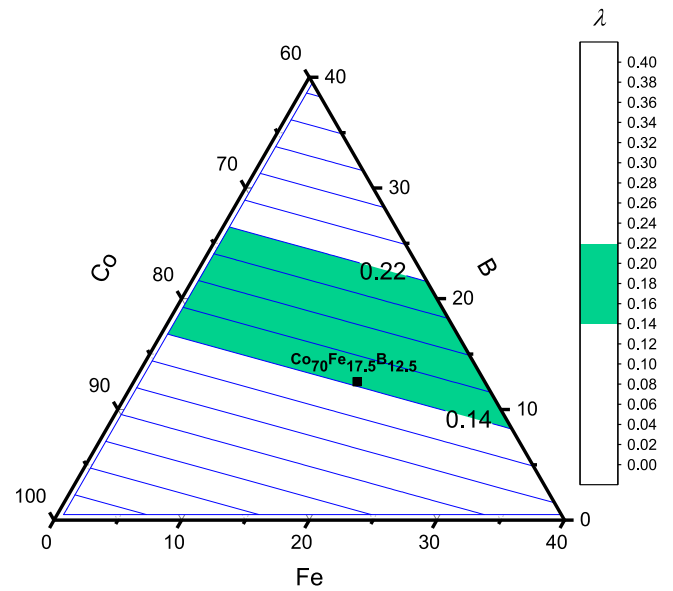

Fig. 3. Variation of atomic mismatch factor in the Co-rich corner of the Co-Fe-B system. Compositions on the blue lines have the same λ. The green region represents the compositions with optimal glass-forming ability.
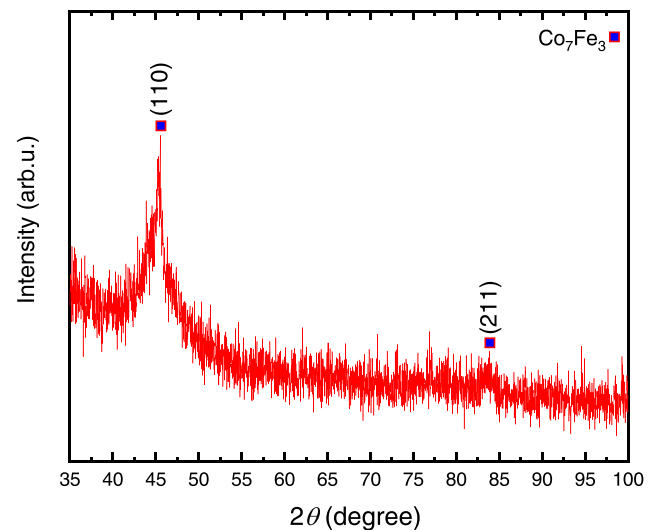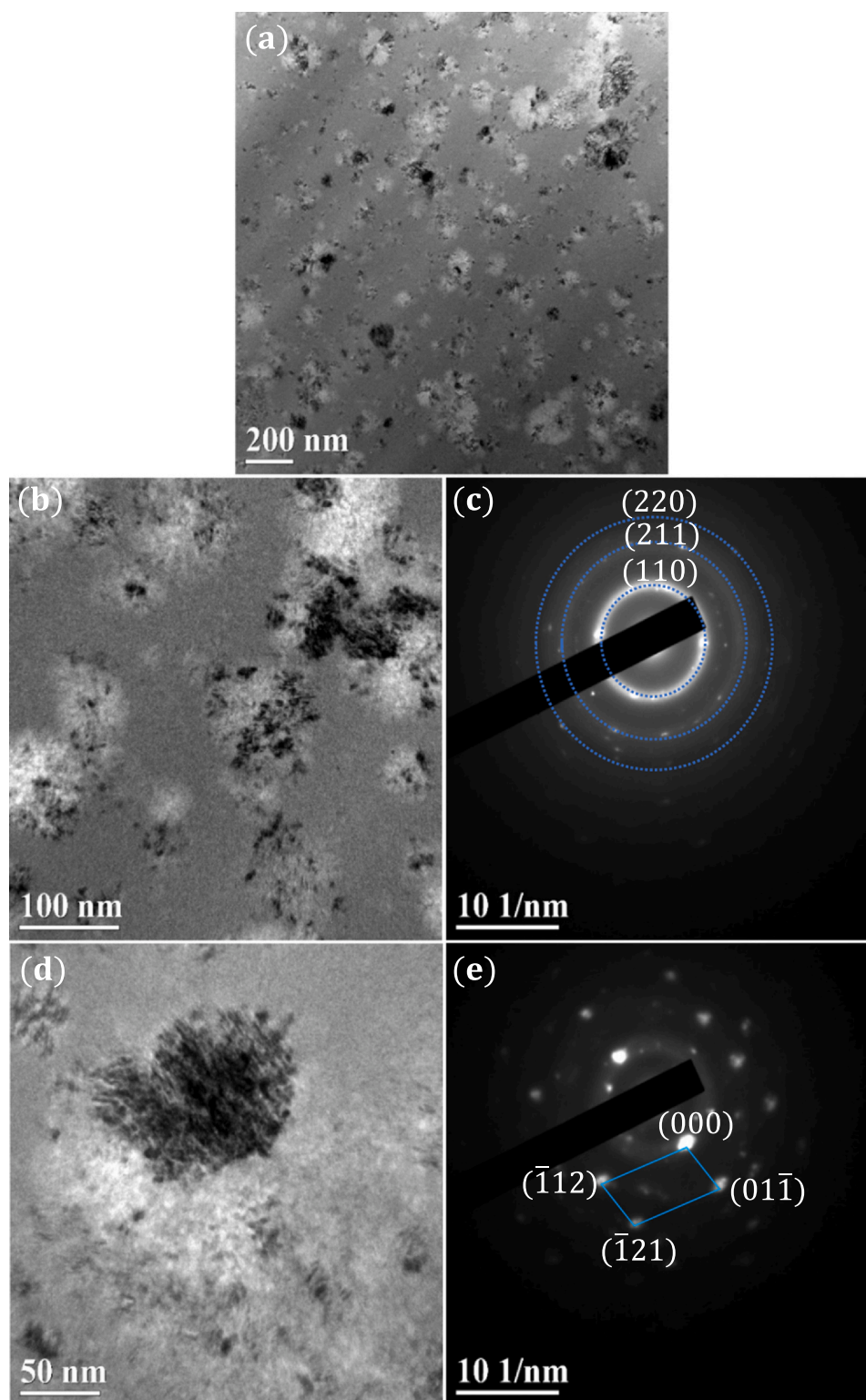

Fig. 4. The X-ray diffraction pattern of the wheel-side of the as-quenched $Co_{70}Fe_{17.5}B_{12.5}$ ribbons.

3.2. Structural characterisation

Fig. 4 shows the XRD pattern of the wheel-side of the as-quenched $Co_{70}Fe_{17.5}B_{12.5}$ ribbons. A sharp Bragg peak at 45.27° <110> and a broader diffused peak at 83.82° <211> can be seen in the XRD pattern, which both represent the Co_7Fe_3 phase formed on the side which experienced higher cooling rate (copper wheel side). Additionally, a sample from the middle region of the cross-section of the ribbon has been examined by TEM to corroborate the local nanocrystalline microstructure. Fig. 5a shows a typical TEM image of the nanocrystals in the glassy matrix. The Selected Area Electron Diffraction (SAED) pattern (Fig. 5c), shows the presence of a typical amorphous halo ring pattern, from the matrix, with discrete diffraction spots corresponding to {110}, {211}, and {220} reflections confirming the presence of the $Im\bar{3}m$ structured Co_7Fe_3 phase. Most of the equiaxed, rather than dendritic, nanocrystalline grains are smaller than 100 nm in size. These results confirm the *in-situ* formation of Co_7Fe_3 nanocrystals in $Co_{70}Fe_{17.5}B_{12.5}$ ribbons. It is worth

Fig. 5. (a), (b), and (d): TEM micrographs of as-quenched nanostructured ribbons in different magnifications, (c) and (e) SAED pattern of (b) and (d) images.

noting that as XRD was performed on the wheel-side and the TEM sample was from the middle of the cross-section of the ribbon, the *in-situ* nanocrystallisation is a volumetric phenomenon, instead of surface crystallisation which possibly can start due to the lower cooling rates at the air-side of the ribbons. The surface crystallisation takes place when the alloy is not well designed with large AMC [27]. The volumetric formation of *in-situ* nanocrystallisation is essential to get the advantage of the high-flux density of the alloys.

In addition, a higher magnified TEM image of nanocrystals and corresponding SAED can be seen in Fig. 5d and e. The latter corresponds to [311]-bcc zone-axis pattern. Diffractions related to different atomic planes are indicated in Fig. 5e. The lattice parameter based on this lattice spacing between different atomic planes is in good agreement with the lattice parameter calculated from the Rietveld refinement analysis of the XRD pattern (Fig. 4). Thus, the observation of this pattern is also a strong evidence of the existence

Table 1

Thermodynamically predicted equilibrium and non-equilibrium phases of $Co_{70}Fe_{17.5}B_{12.5}$ stable at room temperature.

	Equilibrium conditions		Non-equilibrium conditions	
	Phase	Percentage	Phase	Percentage
Stable phases at RT	$(Co,Fe)_3B$	44	$(Co,Fe)_3B$	49.97
	BCC (Co,Fe) S.S.[a]	34	FCC (Co,Fe) S.S.	50
	HCP (Co,Fe) S.S.	22	$(Co,Fe)_2B$	0.03

[a] S.S. stands for solid solution.

of crystalline bcc-Co_7Fe_3 clusters in the as-quenched melt-spun $Co_{70}Fe_{17.5}B_{12.5}$ ribbon. It can also be noted that the background noise seen in the SAED patterns comes from weak scattering by atomic clusters (several atoms in size) in the amorphous matrix surrounding crystalline clusters. Interestingly, the nanocrystalline structure yields in high electrical resistivity (168 μΩ cm) of the alloy. The electrical resistivity of the nanocrystalline materials is higher than both coarse-grained polycrystalline metals and amorphous alloys due to the increased volume fraction of atoms lying at the grain boundaries [28].

Additionally, some thermodynamic and kinetic aspects of these phase transitions are studied below. First, the phase transitions are studied by evaluating the equilibrium and non-equilibrium solidification simulation of the alloy composition using the Pandat™ software. As can be seen in Table 1, five different phases are predicted to crystallise as a result of equilibrium and non-equilibrium solidification of $Co_{70}Fe_{17.5}B_{12.5}$ alloy. Among these phases, $(CoFe)_3B$ has minimum Gibbs energy of formation, −30 kJ/mol. However, the nanocrystals of metastable Co_7Fe_3 form during melt-spinning, and they are stable at room temperature. Thus, this discrepancy between experiment and thermodynamic modelling should be addressed accordingly.

The nucleation of a metastable phase could likely to be more kinetically-favoured compared to that of the stable phase [29]. According to classical nucleation theory [30], the activation threshold for the formation of a critical nucleus is ΔG^*, which is the free energy required to form the critical nucleus;

$$\Delta G^* = \frac{16\pi\sigma^3}{3\Delta G_v^2} f(\theta) \tag{4}$$

where $f(\theta)$ is the catalytic potency factor for heterogeneous nucleation, which depends on the wetting angle θ. ΔG_v is the Gibbs free energy difference between the liquid and the solid:

$$\Delta G_v = \Delta H_f \frac{T_m - T}{T_m} \tag{5}$$

where ΔH_f, T_m, and T denote the enthalpy of fusion, melting temperature, and undercooling temperature, respectively. The interface energy σ can be estimated by the model developed by Spaepen and Meyer [31]:
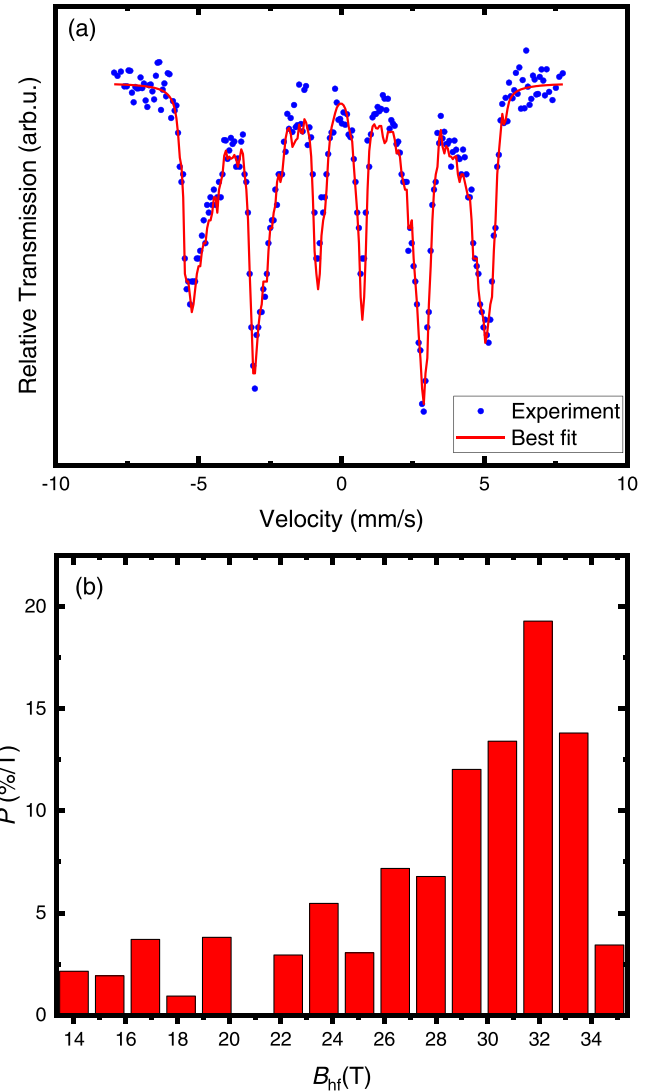
$$\sigma = \alpha \frac{\Delta S_f T}{(N_L V_m^2)^{1/3}} \tag{6}$$

where α is a factor dependent on the structure of the solid nucleus and ΔS_f, N_L; and V_m are the entropy of fusion, Avogadro's number, and the molar volume of the phase, respectively. Without the knowledge of the contact angle θ of the crystal nucleus to the substrate, the nucleation is assumed to be homogenous. Based on this theory, the activation threshold of the dominant stable and possibly metastable phases in this system is estimated and shown in Table 2. As can be seen, the necessary activation energy for the formation of Co_7Fe_3 is about three orders of magnitude less than the one for

Table 2

Gibbs free energy (ΔG_v) and interface energy (σ) difference between the liquid and solid, and the activation threshold for formation of a critical nucleus (ΔG^*) at room temperature.

Phase	ΔG_v (kJ/mol)	σ (J/m^2) × 10^5	ΔG^* (J) × 10^{23}	ΔG^* (meV)
$(CoFe)_3B$	52.34	1.99	4.85	0.3
Co_7Fe_3	12.55	1.39	0.003	0.00019

Fig. 6. (a) Room-temperature Mössbauer spectra, and (b) hyperfine magnetic field distributions of as-quenched $Co_{70}Fe_{17.5}B_{12.5}$.

$(CoFe)_3B$. Therefore, from the kinetics point of view, the nucleation of this phase is more favourable.

3.2.1. Mössbauer spectra of nanostructured alloy

Fig. 6 presents the Mössbauer transmission spectra of $Co_{70}Fe_{17.5}B_{12.5}$ nanocomposite ribbons, along with respective distribution $P(B_{hf})$ of Hyperfine Magnetic Field (HMF). The shape of the spectra is characteristic of a nanocomposite structure with a ferromagnetic arrangement. Thus, both building blocks of the microstructure, nanocrystals and amorphous matrix, can be scrutinised based on the correlated distribution of HMF.

3.2.1.1. Local atomic order in nanocrystals. The hyperfine interaction distribution can be analysed based on the local environment model [32], which has been reported for different ternary systems [33–36].

In Fe–X, where X is treated as an impurity, and it can include different types of elements, every atom X which substitutes iron atom in the ith coordination sphere (or neighbour shell) of the ^{57}Fe isotope causes the change of the HMF at ^{57}Fe site by the value of ΔB_i. The changes in the HMF of iron, as ΔB_i, are additive. In practice, the contributions from the first and the second coordination spheres are considered, and the value $B(m,n)$ of the hyperfine magnetic field at ^{57}Fe site can be described as [37]:

$$B(m, n) = B(0, 0) + m\Delta B_1 + n\Delta B_2 \tag{7}$$

where $B(0,0)$ denotes the value of the HMF at ^{57}Fe nucleus, which is surrounded only by *Fe* atoms in the first and the second coordination spheres; m and n represent the number of impurity atoms in the first and the second sphere, rspectively; the changes of the HMF caused by impurity atoms in the first and the second neighbour shells, respectively. The values of ΔB_1 and ΔB_2 could be positive or negative. Relation (7) has been used for both disordered and ordered alloys in the broad range of impurity concentration [37].

In the FeCo, B2 structural type, there are eight cobalt atoms in the first sphere around an iron atom which is the same as the atomic orientation in Co_7Fe_3. However, there are just two iron atoms in the second sphere in Co_7Fe_3 compared to 6 iron atoms in the FeCo B2 structure. Thus, based on the fact that there are four fewer iron atoms in the second sphere in the Co_7Fe_3 phase and the as-mentioned local environment model, the HMF of Co_7Fe_3, based on its counterpart in FeCo, can be calculated as:

$$B_{Co_7Fe_3} = B_{FeCo} - 4\Delta B_{2,Fe} \tag{8}$$

B_{FeCo} is mentioned to be 34.3 T [38] and ΔB for an iron atom in the second sphere is measured to be 0.77 T [39], so based on Eq. (8), the HMF for an iron atom in Co_7Fe_3 is 31.22 T. This number is close to two peaks of the hyperfine field distributions, at 31 ($P(B_{hf})$ = 13.41%) and 32 ($P(B_{hf})$ = 19.29%) (Fig. 6b). The sum of probabilities for these two fields is 32.7, which agrees with the portion of nanocrystals formed in the amorphous matrix calculated based on the TEM image in Fig. 5a.

3.2.1.2. Local atomic order in the amorphous matrix.
A relatively large portion of the structurally disordered matrix, about 70% (Fig. 5a), leads to the broadening of the experimental HMF peak and a significant contribution of low-field background in the total HMF distribution (Fig. 6b). For every HMF filed (B_{hf}), excluding the ones correlated to Co_7Fe_3 nanocrystals, the number of cobalt and boron atoms in the first sphere around the iron atom can be estimated based on the following Equation [33,37]:

$$B_{hf} = B(0, 0) + m\Delta B_{1,Co} + n\Delta B_{1,B} \tag{9}$$

where m and n denote the numbers of Co and B atoms in the first coordination sphere, while $\Delta B_{1,Co}$ and $\Delta B_{1,B}$ denote changes of the HMF caused by a single Co and B atoms respectively. Statistically, the probability of finding n of Co atoms and m of B atoms in the first coordination shell of ^{57}Fe in the amorphous matrix can be calculated using multinomial distribution [33,37]:

$$P(m, n) = \frac{N!}{m!n!(N - m - n)!} x^m y^n (1 - x - y)^{N-m-n} \tag{10}$$

where N is the number of all atoms in the first coordination sphere, x and y denote the chemical concentration of the cobalt and boron in the amorphous matrix. Among different pairs of m and n, the ones with the highest $P(m, n)$ are chosen. Then $\langle m \rangle$ and $\langle n \rangle$ are calculated based on:

$$\langle m \rangle = \sum m P_{exp}(m, n) \tag{11}$$

$$\langle n \rangle = \sum n P_{exp}(m, n) \tag{12}$$

where P_{exp} denotes the probability of the configuration (m, n) of impurity atoms obtained from the analysis of the experimental Mössbauer spectra. Therefore, the Warren–Cowley parameters for cobalt (α_{Co}) and boron (α_B) atoms have the following form [33,37]:

$$\alpha_{Co} = \frac{\langle m \rangle - 8x}{8(1 - x)} \tag{13}$$

$$\alpha_B = \frac{\langle n \rangle - 8y}{8(1 - y)} \tag{14}$$

The interpretation of the values of the Warren–Cowley parameters is as follows: when $\alpha_i = 0$ then the distribution of impurity atoms is random; if $\alpha_i < 0$ the impurity atoms form clusters, *i.e.* they attract each other, and finally when $\alpha_i > 0$; the impurity atoms undergo the short-range order (SRO) effect, *i.e.* they are attracted by the matrix atoms [33,37]. Based on this theory, cobalt atoms cluster as $\alpha_{Co} = -1.17$. As the most stable local configuration of cobalt is highly dense hcp, this element shows the high tendency for clustering in a large variety of systems with either metallic or covalent bonding. The strong drive for clusterisation of the cobalt atoms, which leads to a local increase in their concentration, in addition to the tendency of boron atoms to undergo SRO leads to the nucleation of ordered cobalt-rich Co_7Fe_3 phase (Figs. 4 and 5). Warren–Cowley parameter for boron atoms is 0.12, implying that they, indeed, undergo SRO. A repulsive potential between the small boron atoms and attraction between the boron atoms and large cobalt/iron atoms could lead to the formation of a tetrahedron of four cobalt/iron atoms 'stuffed with boron', minimising the voids in the Bernal dense random packing structure [40], and thereby stabilising the structure against easy crystallisation.

3.3. Magnetic properties

The evolution of magnetisation, measured along the length of the ribbons, as a function of the applied magnetic field, is presented in Fig. 7. It can be seen that the coercivity, $H_c = 381.5$ A/m, and the anisotropy field, $H_k = 728.5$ A/m, are high which could be attributed to the effect of magnetocrystalline anisotropy of the ordered nanocrystals of the Co_7Fe_3 phase. The as-mentioned effect can be measured quantitatively, by the anisotropy energy (K_u), which is calculated based on the following Equation [41]:
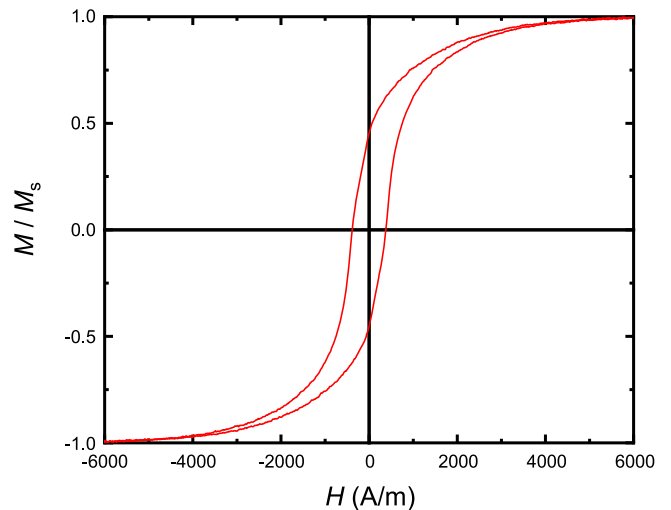
$$K_u = \frac{H_k \mu_0 M_s}{2} \tag{15}$$

Fig. 7. Hysteretic loop of as-quenched nanocrystalline $Co_{70}Fe_{17.5}B_{12.5}$ ribbons, $\mu_0 M_s = 1.57$ T.

where μ_0 is the free space permeability. The anisotropy is related to directional atomic ordering along the direction of the local magnetisation to minimise the spin-orbit coupling energy [42]. The calculated anisotropy energy for the *in-situ* nanocrystalline alloy is 573 J/m^3, which is about twenty times larger than the values reported for similar amorphous alloys [3]. Furthermore, the M_s of the *in-situ* nanocrystalline alloy is 1.57 T. The relatively high M_s is due to the presence of the ordered Co$_7$Fe$_3$ phase, which its M_s is ~4% higher than its disordered counterparts [43]. High M_s of Co$_7$Fe$_3$ can also be inferred from the high hyperfine magnetic field interactions of the Fe nuclei, in the nanocrystals of Co$_7$Fe$_3$ (Fig. 6b).

To understand the evolution of M_s of the alloy, it is necessary to take into account a few primary considerations concerning the electronic structure and magnetic properties of the 3d system. In this regard, the Slater–Pauling figure, which shows the relationship between the magnetic moment and the number of valence electron per atom (e/a) is used. The e/a is estimated for Co$_7$Fe$_3$ nanocrystals, as 8.71, and for the amorphous matrix 7.72. Then, e/a for the nanocomposite is calculated based on the portion of the nanocrystals in the amorphous matrix. The magnitude of the magnetic moment for e/a of the nanocomposite is 1.64 μ_B which is slightly higher than the magnetic moment of the nanocomposite estimated based on M_s, 1.47 μ_B. This difference can be due to the hybridisation effect, as a result of SRO of boron atoms, which is observed by Mössbauer spectroscopy in Section 3.2.1.

4. Conclusions

An *in-situ* nanocrystallised Co$_{70}$Fe$_{17.5}$B$_{12.5}$ alloy, with a tuned amorphisation capability has been designed, using a thermodynamics-based CALPHAD approach, together with a topological instability parameter. The proposed scheme works as a guideline for the tuning of AMC of alloys, to favour the formation of the desired ordered phase (Co$_7$Fe$_3$) nanocrystals throughout the volume of the alloys, during the rapid quenching process. This can be achieved without any post-spinning heat treatment, which is normally required in order to grow the necessary amount of nanocrystalline phase. The XRD and TEM results confirm the formation of the Co$_7$Fe$_3$ ordered phase, dispersed heterogeneously throughout the amorphous matrix. Furthermore, the local atomic order of the nanocrystalline structures and the amorphous matrix has been investigated by the distribution of hyperfine magnetic field, using Mössbauer spectroscopy. In the latter, the Warren–Cowley parameter is negative for cobalt atoms showing their tendency to form ordered structures, and it is positive for boron atoms implying that they are prone to undergo short-range order due to their size and electronegativity difference with atoms in the amorphous matrix. The proposed approach of designing *in-situ* nanocrystalline alloys by rapid quenching, using both thermodynamic and topological parameters, is useful for the development of functional materials for a broad range of applications. Future research on the introduction of other elements, such as Nb or Cu, in order to increase the number of crystalline nuclei in the two-phase system (melt-solid) and therefore further decrease the grain size, may also benefit from the proposed predictive modelling approach.

CRediT authorship contribution statement

Hasan Ahmadian Baghbaderani: Methodology, Validation, Formal analysis, Investigation, Data curation, Writing - original draft, Visualization. **Ansar Masood:** Conceptualization, Methodology, Validation, Formal analysis, Investigation, Resources, Data curation, Writing - review & editing, Project administration, Funding acquisition. **Kenny L. Alvarez:** Investigation, Data curation, Writing - review & editing. **Cian Ó Mathúna:** Supervision. **Paul McCloskey:** Conceptualization, Validation, Project administration, Writing -

review & editing, Funding acquisition. **Plamen Stamenov:** Conceptualization, Validation, Project administration, Writing - review & editing, Formal analysis, Visualization, Funding acquisition.

Declaration of Competing Interest

The authors declare that they have no known competing financial interests or personal relationships that could have appeared to influence the work reported in this paper.

Acknowledgement

References

[1] A.D.M. Charles, A.N. Rider, S.A. Brown, C.H. Wang, Multifunctional magneto-polymer matrix composites for electromagnetic interference suppression, sensors and actuators, Prog. Mater. Sci. 115 (2021) 100705, https://doi.org/10.1016/j.pmatsci.2020.100705

[2] K.J. Overshott, Soft magnetic materials, Phys. Technol. 6 (1975) 280–281, https://doi.org/10.1088/0305-4624/6/6/409

[3] H. Ahmadian Baghbaderani, A. Masood, Z. Pavlovic, K.L. Alvarez, C. ÓMathúna, P. McCloskey, P. Stamenov, On the mechanisms limiting power loss in amorphous CoFeB-based melt-spun ribbons, J. Magn. Magn. Mater. 502 (2020) 166535, https://doi.org/10.1016/j.jmmm.2020.166535

[4] K.L. Alvarez, H.A. Baghbaderani, J.M. Martín, N. Burgos, M. Ipatov, Z. Pavlovic, P. McCloskey, A. Masood, J. Gonzalez, Novel Fe-based amorphous and nanocrystalline powder cores for high-frequency power conversion, J. Magn. Magn. Mater. 501 (2020) 166457, https://doi.org/10.1016/j.jmmm.2020.166457

[5] A. Masood, H.A. Baghbaderani, V. Ström, P. Stamenov, P. McCloskey, C.Ó. Mathúna, S. Kulkarni, Fabrication and soft magnetic properties of rapidly quenched Co-Fe-B-Si-Nb ultra-thin amorphous ribbons, J. Magn. Magn. Mater. 483 (2019) 54–58, https://doi.org/10.1016/j.jmmm.2019.03.079

[6] A. Masood, H.A. Baghbaderani, K.L. Alvarez, J.M. Blanco, Z. Pavlovic, V. Ström, P. Stamenov, C.O. Mathuna, P. McCloskey, High-frequency power loss mechanisms in ultra-thin amorphous ribbons, J. Magn. Magn. Mater. (2020) 167469, https://doi.org/10.1016/j.jmmm.2020.167469

[7] O. Gutfleisch, M.A. Willard, E. Brück, C.H. Chen, S.G. Sankar, J.P. Liu, Magnetic materials and devices for the 21st century: stronger, lighter, and more energy efficient, Adv. Mater. 23 (2011) 821–842, https://doi.org/10.1002/adma.201002180

[8] D. Raskin, C.H. Smith, Chapter 20 – Applications of amorphous metals: progress and prospects A2, in: F.E. Luborsky (Ed.), Amorphous Metallic Alloys, Butterworth-Heinemann, 1983, pp. 381–400, https://doi.org/10.1016/B978-0-408-11030-3.50025-X

[9] C.Ó. Mathúna, N. Wang, S. Kulkarni, S. Roy, Review of integrated magnetics for power supply on chip (PwrSoC), IEEE Trans. Power Electron. 27 (2012) 4799–4816, https://doi.org/10.1109/TPEL.2012.2198891

[10] M. Najafi, F. Hayati, A.A. Rafati, Effect of current frequency and annealing on magnetic properties of [Co70Fe30]97Sn3 nanowire arrays, in: Proceedings of the International Conference – Nanomaterials: Applications & Properties, 1, 2012, 04MFPN10-2. ⟨http://essuir.sumdu.edu.ua/retrieve/76719/princon_2012_1_4_27.pdf⟩.

[11] S. Amsarajan, B.R. Jagirdar, Air-stable magnetic cobalt-iron (Co7Fe3) bimetallic alloy nanostructures via co-digestive ripening of cobalt and iron colloids, J. Alloy. Compd. 816 (2020) 152632, https://doi.org/10.1016/j.jallcom.2019.152632

[12] J.G. Wang, H. Zhao, C.X. Xie, C.T. Chang, S.M. Zhou, J.Q. Feng, J.T. Huo, W.H. Li, In-situ synthesis of nanocrystalline soft magnetic Fe-Ni-Si-B alloy, J. Alloy. Compd. 790 (2019) 524–528, https://doi.org/10.1016/j.jallcom.2019.03.226

[13] S.V. Thomas, M.A. Willard, A. Martone, M.J. Heben, V. Solomon, A. Welton, P. Boolchand, R.C. Ewing, C. Wang, S.L. Bud'ko, J. Song, D. Shi, Nanocrystallites via direct melt spinning of Fe77Ni5.5Co5.5Zr7B4Cu for enhanced magnetic softness, Phys. Status Solidi Appl. Mater. Sci. 217 (2020) 1–10, https://doi.org/10.1002/pssa.201900680

[14] A.I.C. Suryanarayana, Bulk Metallic Glasses, Second edition, CRC, New York, 2012.

[15] J. Bhatt, W. Jiang, X. Junhai, W. Qing, C. Dong, B.S. Murty, Optimization of bulk metallic glass forming compositions in Zr–Cu–Al system by thermodynamic modeling, Intermetallics 15 (2007) 716–721, https://doi.org/10.1016/j.intermet.2006.10.018

[16] D.D.E.E. Brennhaugen, H. Mao, D.V. Louzguine-Luzgin, L. Arnberg, R.E. Aune, Predictive modeling of glass forming ability in the Fe-Nb-B system using the CALPHAD approach, J. Alloy. Compd. 707 (2017) 120–125, https://doi.org/10.1016/j.jallcom.2016.12.049

[17] A. Tabeshian, H. Mao, L. Arnberg, R.E. Aune, Investigation of glass forming ability in the Zr-rich part of the Zr-Fe-Al ternary system, J. Appl. Phys. 125 (2019) 8–15, https://doi.org/10.1063/1.5066554

[18] D. Turnbull, Under what conditions can a glass be formed? Contemp. Phys. 10 (1969) 473–488, https://doi.org/10.1080/00107516908204405

[19] ASM Handbook, ASM-Alloy Phase Diagrams, Volume 3, ASM International, 1992. pdf, (n.d.).

[20] A. Inoue, High strength bulk amorphous alloys with low critical cooling rates (overview), Mater. Trans. JIM 36 (1995) 866–875, https://doi.org/10.2320/matertrans1989.36.866

[21] J.W. Martin, Glasses and ceramics, Materials for Engineering, Third edition, Woodhead Publishing, 2006, pp. 133–158.

[22] A. Takeuchi, A. Inoue, Calculations of mixing enthalpy and mismatch entropy for ternary amorphous alloys, Mater. Trans. JIM 41 (2000) 1372–1378, https://doi.org/10.2320/matertrans1989.41.1372

[23] J. Guo, X. Bian, X. Li, C. Zhang, Evaluation of liquid fragility for glass-forming alloys based on mixing enthalpy and mismatch entropy, Intermetallics 18 (2010) 933–937, https://doi.org/10.1016/j.intermet.2010.01.004

[24] R. Lisboa, C. Bolfarini, W. Botta, C. Kiminami, Topological instability as a criterion for design and selection of aluminum-based glass-former alloys, Appl. Phys. Lett. 86 (2005) 211904, https://doi.org/10.1063/1.1931047

[25] Z.J. Yan, J.F. Li, S.R. He, Y.H. Zhou, Evaluation of the optimum solute concentration for good glass forming ability in multicomponent metallic glasses, Mater. Res. Bull. 38 (2003) 681–689, https://doi.org/10.1016/S0025-5408(03)00010-2

[26] T. Egami, Y. Waseda, Atomic size effect on the glass forming ability of metallic alloys, J. Non-Cryst. Solids 64 (1984) 113–134.

[27] J. Zhang, F. Wan, Y. Li, J. Zheng, A. Wang, J. Song, M. Tian, A. He, C. Chang, Effect of surface crystallization on magnetic properties of Fe82Cu1Si4B11.5Nb1.5 nano-crystalline alloy ribbons, J. Magn. Magn. Mater. 438 (2017) 126–131, https://doi.org/10.1016/j.jmmm.2017.04.086

[28] C. Suryanarayana, Nanocrystalline materials, Int. Mater. Rev. 40 (1995) 41–64, https://doi.org/10.1179/imr.1995.40.2.41

[29] X.X. Wei, W. Xu, J.L. Kang, M. Ferry, J.F. Li, Metastable Co23B6 phase solidified from deeply undercooled Co79.3B20.7 alloy melt, J. Mater. Sci. 51 (2016) 6436–6443, https://doi.org/10.1007/s10853-016-9941-4

[30] D.A. Porter, K.E. Easterling, M.Y. Sherif, Phase Transformations in Metals and Alloys, Third edition, (2009).

[31] F. Spaepen, R.B. Meyer, The surface tension in a structural model for the solid-liquid interface, Scr. Metall. 10 (1976) 37–43, https://doi.org/10.1016/0036-9748(76)90323-9

[32] M. Rubinstein, Hyperfine field spectra of binary Fe-Co alloys: nuclear magnetic resonance of ^{57}Fe and ^{59}Co, Phys. Rev. 172 (1968) 277–283, https://doi.org/10.1103/PhysRev.172.277

[33] T. Pikula, Local atomic arrangement in mechanosynthesized CoxFe1−x−yNiy alloys studied by Mössbauer spectroscopy, Appl. Phys. A Mater. Sci. Process. 117 (2014) 1491–1498, https://doi.org/10.1007/s00339-014-8582-1

[34] C. Djega-Mariadassou, L. Bessais, C. Servant, Nanocrystalline precipitates formed by aging of bcc disordered Fe-Ni-Mo alloys, Phys. Rev. B 51 (1995) 8830–8840, https://doi.org/10.1103/PhysRevB.51.8830

[35] J.M. Grenèche, Local structural order in disordered systems investigated by Mössbauer spectrometry, J. Non-Cryst. Solids 287 (2001) 37–44, https://doi.org/10.1016/S0022-3093(01)00634-2

[36] J. Restrepo, G.A. Pérez Alcázar, Interpretation based on a binomial method of the hyperfine field distributions of disordered: Fe0.9−xMn0.1Alx alloys, J. Magn. Magn. Mater. 213 (2000) 135–142, https://doi.org/10.1016/S0304-8853(99)00541-7

[37] E. Jartych, Local atomic order in nanocrystalline Fe-based alloys obtained by mechanical alloying, J. Magn. Magn. Mater. 265 (2003) 176–188, https://doi.org/10.1016/S0304-8853(03)00263-4

[38] Q. Samara, S.H. Mahmood, On the magnetic properties and hyperfine fields in Fe-containing alloys: a theoretical study, Phys. Status Solidi (c) 3291 (2006) 3285–3291, https://doi.org/10.1002/pssc.200567119

[39] Z. Klencsár, P. Németh, Z. Sándor, T. Horváth, I.E. Sajó, S. Mészáros, J. Mantilla, J.A.H. Coaquira, V.K. Garg, E. Kuzmann, G. Tolnai, Structure and magnetism of Fe-Co alloy nanoparticles, J. Alloy. Compd. 674 (2016) 153–161, https://doi.org/10.1016/j.jallcom.2016.03.068

[40] D.E. Polk, The structure of glassy metallic alloys, Acta Metall. 20 (1972) 485–491, https://doi.org/10.1016/0001-6160(72)90003-X

[41] F. Johnson, C.Y. Um, M.E. McHenry, H. Garmestani, The influence of composition and field annealing on magnetic properties of FeCo-based amorphous and na-nocrystalline alloys, J. Magn. Magn. Mater. 297 (2006) 93–98, https://doi.org/10.1016/j.jmmm.2005.02.056

[42] R.C. O'Handley, Modern Magnetic Materials: Principles and Applications, Wiley, 1999, ⟨https://books.google.ie/books?id=RKV1QgAACAAJ⟩.

[43] D.W. Clegg, R.A. Buckley, The disorder ⇌ order transformation in iron-cobalt-based alloys, Met. Sci. J. 7 (1973) 48–54, https://doi.org/10.1179/030634573790445541